Defect levels and hyperfine constants of hydrogen in beryllium oxide from hybrid-functional calculations and muonium spectroscopy

A. G. Marinopoulos,[a)] R. C. Vilão, R. B. L. Vieira, H. V. Alberto, and J. M. Gil

CFisUC, Department of Physics, University of Coimbra, P-3004-516 Coimbra, Portugal

M. V. Yakushev

Department of Physics, SUPA, University of Strathclyde, Glasgow G4 0NG, UK

Ural Federal University, Ekaterinburg 620002, Russia and

Institute of Solid State Chemistry of the Urals branch of the RAS, Ekaterinburg 620990, Russia

R. Scheuermann and T. Goko

Laboratory for Muon Spectroscopy, Paul Scherrer Institute, CH-5232, Villigen, Switzerland

(Dated: 3 December 2016)

The atomistic and electronic structures of isolated hydrogen states in BeO were studied by ab initio calculations and muonium spectroscopy (μSR). Whereas standard density-functional theory with a semi-local GGA functional led to a detailed probing of all possible minimum-energy configurations of hydrogen further calculations with the hybrid HSE06 functional provided improved properties avoiding band-gap and self-interaction errors. Similarly to earlier findings for the other wide-gap alkaline-earth oxide, MgO, hydrogen in BeO is also predicted to be an amphoteric defect with the pinning level, E(+/-), positioned in the mid-gap region. Both donor and acceptor levels were found too deep in the gap to allow for hydrogen to act as a source of free carriers. Whereas, hydrogen in its positively-charged state, H^+, adopts exclusively hydroxide-bond OH configurations, H^0 and H^- instead show a preference to occupy cage-like interstitial sites in the lattice. H^0 in particular displays a multitude of minimum-energy configurations: its lowest-energy ground state resembles closely a trapped-atom state with a nearly spherical spin-density profile. In contrast to the strongly ionic MgO, H^0 in BeO was further found to stabilize in additional higher-energy elongated-bond OH configurations whose existence should be traced to a partial covalent character of the Be-O bonding. Calculations of the proton-electron hyperfine coupling for all H^0 states showed that the ground-state interstitial H^0 configuration is dominated by an isotropic hyperfine interaction with a magnitude very close to the vacuum value, a finding corroborated by the μSR-spectroscopy data.

PACS numbers: 71.15.Nc, 71.55.-i, 71.15.Mb, 76.75.+i

[a)] agmarinopoulos@gmail.com

I. INTRODUCTION

BeO is an alkaline-earth oxide with diverse applications as a structural ceramic.[1] It crystallizes in the hexagonal wurtzite structure at ambient conditions and, in contrast to the strongly ionic MgO, it also possesses a small covalent character of bonding.[2,3] The combination of its band gap of 10.6 eV, its optical transparency over a broad spectral range from 121 to 7000 nm with a high melting point of 2500° C and thermal conductivity of 330 $WK^{-1}m^{-1}$ (one of the highest thermal conductivities among non metals[4]), as well as its high radiation hardness provide an excellent potential for very different applications like optical windows, dosimetry systems,[5] heat sinks, rocket engines, crucibles and thermocouple tubing. Other applications include its use in the energy production and nuclear fusion as the material of the inner walls containing the deuterium-tritium plasma in tokamaks.[6] Recently[7] BeO has also been proposed as an interfacial passivation layer adjacent to the high-κ dielectric in microelectronic devices: it is thermodynamically stable in contact with silicon and acts as a good diffusion barrier. The Si/BeO interface, in particular, was found to exhibit a higher barrier to tunneling and thermionic leakage currents than those with alumina and HfO_2. Favorable electrical characteristics of Si/BeO MOS devices were also reported.[8]

The promising use of BeO in high-κ technology and microelectronics brings forth the effect of hydrogen, arguably among the major impurities causing serious reliability issues in the corresponding devices.[9–12] Recently, hydrogen was suggested to be a two-level system defect in atomic layer deposition (ALD) BeO.[13] In undoped BeO ALD thin films, H concentration was measured to be as high as 4%.[14] These high concentrations are bound to impact deeply on the properties of the material. An essential first step in order to understand the effect of hydrogen is the characterization of the microscopic configurations of isolated hydrogen in the host oxide.

Unfortunately important aspects of the nature and behavior of isolated hydrogen in BeO, in particular its electronic structure and related properties are still to be studied by either theoretical or experimental means. First-principles calculations of hydrogen states based on density-functional theory (DFT)[15,16] within the generalized-gradient approximation (GGA)[17] were performed recently[6] but they were restricted to the neutral charge state, thus no charge-transition (electrical) levels were reported. Hydrogen was found to reside in an insterstitial site in the lattice inducing a deep level in the lower half of the band gap.[6]

Experimentally, isolated hydrogen is extremely difficult to characterize in a direct way. Yet, muonium spectroscopy can provide detailed information about the electronic structure of muonium/hydrogen, through the hyperfine interaction, using muonium as a light pseudo-isotope of hydrogen.[18–20] Such information is almost non-existent for isolated hydrogen from any other technique.[20] The μSR results compare well with those obtained directly with protons, for the very few cases allowing comparison.[20,21] For the case of BeO no published studies based on μSR exist, with the exception of an unpublished communication from an early conference where an atomic-like muonium state was reported.[22]

In the present study we adopted a synergistic approach comprising both first-principles calculations and μSR spectroscopy in order to characterize isolated hydrogen states in BeO in a manner similar to what was done previously in paratellurite (α-TeO_2),[23] yttria,[24] lutetium oxide[25] and zirconia,[26] thus providing a much needed experimental verification of the theoretical predictions. The calculations consisted of a conventional semilocal (GGA) DFT functional supplemented by a hybrid-functional approach. The former was chosen for its computational efficiency which allowed a detailed probing of the configurational space of hydrogen states in the lattice treating the structural relaxation effects present in large defect supercells. Nonetheless, local and semilocal DFT functionals have been known to underestimate the quasiparticle band gaps in solids and are prone to a strong self-interaction error which has lead to spurious delocalization of the electron and hole densities in several studies of defects in oxides.[27–31] The strong underestimation of the experimental band gap of BeO was indeed observed in virtually all previous DFT calculations of the wurtzite phase of BeO within GGA[6,32–34] or within the local-density approximation (LDA).[35–37] Either of these approches led to band gaps in the range from 7 to 8 eV, which were much smaller to the measured BeO band gap (10.6 eV).[38]

A number of recent studies, nonetheless, were able to correct the band-gap problem for BeO. Baumeier and coworkers[37] employed norm-conserving pseudopotentials which incorporated self-interaction corrections leading to a band gap of 10.5 eV. Hybrid functionals (B3LYP) which add exact Hartree-Fock exchange were also used and improved the band gap (10.39 eV).[39] Lately, many-body perturbation theory within the GW_0 approximation (full update of the eigenvalues of the Green's function G to self consistency) also gave a much improved band gap, equal to 10.70 eV.[34]

In the present work, in addition to a semilocal GGA functional, we employed the HSE06

hybrid functional[40–42] where a portion of exact non-local Hartree-Fock exchange is admixed to the semilocal GGA exchange. The HSE06 functional has been shown to provide band gaps in solids in very good agreement with experiment.[42] Using both methodologies we performed a detailed identification of the minimum-energy configurations of hydrogen in the lattice along with their formation energies and charge-transition levels. Induced states in the gap and hyperfine parameters were also calculated for the case of the neutral paramagnetic state, thus allowing fruitful comparisons with the μSR results.

We have modelled hydrogen experimentally using the positive muon as a light pseudo-isotope.[43,44] The characterization of the anticipated atomic-like muonium state is best performed in high-field experiments in transverse geometry, so we have used the recently installed HAL9500 instrument at the Paul-Scherrer Institut, Switzerland, which is specially dedicated to μSR experiments in high magnetic fields.[45] Muon spin rotation measurements were completed on a monocrystalline sample of BeO. During this experiment, magnetic fields up to 8 T were applied across the sample in a direction perpendicular (transverse) to the incoming muon spin polarization direction, at $T = 6$ K. Data analysis was performed with the *musrfit* code.[46]

II. THEORETICAL METHODOLOGY

The first-principles calculations in the present study consisted of two different methods. First, conventional density-functional theory (DFT)[15,16] within the generalized-gradient approximation (GGA) for exchange and correlation. The semilocal PBE[17] density functional was used in this case, an efficient scheme for defective sustems with a large number of atoms. The second method employed was the HSE06 hybrid functional[40–42] where a portion of exact non-local Fock exchange is admixed to the semilocal PBE exchange. A fraction, α, equal to 0.36 of exact exchange was found to reproduce the experimental gap, 10.6 eV,[38] of BeO and was used in the present study.

All calculations were based on the projector augmented-wave (PAW) method[47,48] using pseudopotentials to account for the valence-core interaction. The corresponding implementations currently distributed in the VASP code[49–51] were employed. The crystalline wavefunctions were expanded in a plane-wave basis that was limited by a maximum kinetic-energy cutoff of 470 eV. A Γ-centered $10\times10\times6$ **k**-point mesh was used for the Brillouin-zone

intergrations during the bulk-crystal optimizations. The chosen magnitude of the cutoff was sufficient to achieve convergence in structural properties and defect formation energies. Nonetheless, much larger basis sets (corresponding to a kinetic-energy cutoff of up to 650 eV) were found necessary to attain converged hyperfine parameters for neutral hydrogen. These parameters were determined within the PAW methodology[52,53] by reconstructing the all-electron wavefunctions inside the core regions of the nuclei.

For the defect calculations a 72-atom hexagonal supercell was constructed after suitably repeating the primitive wurtzite BeO cell by 3×3×2 along the **a**, **b** and **c** lattice vectors, respectively. A much coarser Γ-centered 2×2×2 **k**-point mesh was used in this case giving a total of eight non-equivalent **k** points in the Brillouin zone.

The formation energies $E_{\text{form}}(H^q)$ of the various hydrogen configurations were determined for each of its charge states q (q=-1, 0 or +1), as a function of the Fermi-level position E_F in the gap. The corresponding expression is:

$$E_{\text{form}}(H^q) = E_{\text{tot}}(H^q) - E_{\text{tot}}(\text{bulk}) - \mu_H + q(E_F + E_{\text{V}}) \quad (1)$$

where $E_{\text{tot}}(H^q)$ is the total energy of the supercell with hydrogen in the charge state q and $E_{\text{tot}}(\text{bulk})$ the total energy of the bulk-crystal supercell.

μ_H is the chemical potential of hydrogen and in the present study was taken as half the total energy of a hydrogen molecule at T = 0 K. E_{V} is the energy of the valence-band (VB) edge of the bulk supercell and defines the reference energy for the Fermi-level positions in the gap. A correction to the formation energies of the charged states of hydrogen was also added in order to account for the electrostatic interactions of the defect with its periodically generated images. For this purpose, the first-order correction due to Makov and Payne[54] was used. Taking a value of 7.13 for the static dielectric constant from previous experimental studies[55,56] the magnitude of the correction applied was equal to 0.36 eV.

The hyperfine tensor, **A**, is a second-order tensor and describes the interaction of the electron spin with the non-zero magnetic moments of the nuclei.[52,53,57–59] In the present work the calculations of **A** were performed by both PBE and HSE06 functionals and for all distinct paramagnetic H^0 states, taking into account spin polarization. **A** can be generally represented by two parts: by an isotropic term, A_{iso}, also known as the Fermi-contact interaction and a traceless anisotropic term, **B**, as follows:[52,53,57–59]

$$\mathbf{A} = A_{\text{iso}}\mathbf{I} + \mathbf{B} \tag{2}$$

where $\mathbf{I}$ is the 3×3 identity matrix.

A_{iso} is a direct measure of the localization character of the hydrogen electron. The specific value of A_{iso} depends upon the magnitude of the electron spin density ρ_s ($\rho_s = \rho_\uparrow$ - $\rho_\downarrow$) at the site $\mathbf{R}$ of the nucleus as:[52,53,57–59]

$$A_{\text{iso}} = \frac{8\pi}{3} g_e \mu_e g_H \mu_H \rho_s(\mathbf{R}) \tag{3}$$

where: g_e is the electronic g-factor, μ_e the Bohr magneton, g_H the nuclear gyromagnetic ratio for hydrogen and μ_H the nuclear magneton. The contribution of the core spin polarization to the Fermi-contact component was added by means of the frozen valence spin-density approximation.[53] The anisotropic part, $\mathbf{B}$, accounts for the magnetic dipole-dipole interactions between the electron spin and the nuclear magnetic moments.[52,53,57–59] The diagonalization of the hyperfine tensor can then provide the principal values of the hyperfine interaction, labeled as A_{xx}, A_{yy} and A_{zz}. From these values the Fermi-contact term A_{iso} is then obtained as: $\frac{1}{3}$ (A_{xx}+A_{yy}+A_{zz}).

By taking also into account the anisotropic part of the hyperfine tensor the dipolar constant D (frequently also denoted as b in the literature) can also be obtained. The quantity D can be calculated from the principal values of the hyperfine tensor as follows:

$$D = 2b = 2(A_{\parallel} - A_{\perp})/3 \tag{4}$$

with $A_{\parallel}$ being the largest of the principal values (usually A_{zz} by convention) and $A_{\perp}$ the average of the remaining two. The difference in the magnitude of the two smaller principal values reflects the asymmetry of the hyperfine interaction; nonetheless, for all hydrogen configurations studied in the present study this asymmetry was equal to zero ($A_{xx} = A_{yy}$), reflecting the axial symmetry of the respective hyperfine tensors.

III. RESULTS

A. Hydrogen configurations and formation energies

The structural optimization of the BeO primitive unit cell using the semilocal PBE functional led to lattice parameters, a and c equal to 2.715 Å and 4.41 Å, respectively. The internal parameter u was found equal to 0.378. These values reproduce very well the existing experimental measurements[60] of the lattice parameters of the wurtzite phase of BeO: $a = 2.698$ Å and $c = 4.379$ Å. In contrast, the obtained band gap by GGA-PBE, 7.41 eV, underestimates appreciably the experimental gap. The latter was found to be equal to 10.6 eV from optical reflectance data at normal incidence for BeO single crystals.[38]

The hybrid HSE06 functional was also used to optimize the lattice parameters of the bulk crystalline lattice. The optimization was carried out for various values of the Hartree-Fock exchange fraction, α. The optimum magnitude of α was chosen in order to attain the best match with the experimental band gap of BeO. The final fraction was taken equal to 0.36 and led to a direct band gap equal to 10.58 eV at the Γ point. Such a high magnitude of exact Hartree-Fock exchange is consistent with earlier work[61] using the hybrid HSE06 functional where again rather large exact-exchange fractions were needed to reproduce the experimental gaps of wide-gap insulators, in particular sapphire (α=0.29), SiO_2 (α=0.35) and MgO (α=0.40). The final optimized lattice parameters a and c obtained by the HSE06 functional were equal to 2.68 Å and 4.35 Å, respectively. The internal parameter u was again equal to 0.378. Part of the bulk-crystalline cell after structural optimization using the HSE06 functional is displayed in Fig.1(a)). Both Be and O species have a four-fold coordination, with one longer Be-O bond (with a length equal to 1.645 Å) oriented parallel to the **c** axis and three shorter Be-O bonds almost perpendicular to the **c** axis, with a length equal to 1.635 Å.

Hydrogen was initially placed at certain high-symmetry positions in the host lattice, more specifically the bond-center (BC) sites, and the antibonding (AB) positions AB-Be and AB-O (see Fig.1(a)). More general positions of lower symmetry were also tried. The resulting structural optimization was then performed by the PBE functional by minimizing the total supercell energies with respect to all atomic positions. HSE06 was eventually employed to determine the formation energies of the final minimum-energy configurations of hydrogen

for each of its charge states, H^+, H^0 and H^-, taking care to minimize any residual forces.

Hydrogen in its positively-charged state, H^+, adopted exclusively hydroxide-bond configurations with H^+ forming short OH dative bonds with the oxygen ions of the host. Four distinct configurations of such type were determined; two of them with the OH bond oriented parallel to the hexagonal **c** axis, whereas in the other two the OH bond was nearly perpendicular to **c** (see Fig.1).

More specifically: H^+ initially placed at the BC sites was found to be unstable causing strong displacements of the nearest-neighbor Be atom which moved further away from H^+. Very likely this is a consequence of the strong ionicity of BeO with the Be species acting effectively as positively-charged cation which is repelled by H^+. The result of these relaxations is that H^+ eventually forms a dative-type OH bond with the neighboring oxygen of the initial Be-O bond. Two distinct configurations were obtained depending upon the OH bond orientation with respect to the **c** axis; one with the OH bond oriented parallel to **c** (H^+-$OH_{\parallel}$) and the other with the OH bond oriented nearly perpendicular to **c** (H^+-$OH_{\perp}$) (see Fig. 1(b) and Fig. 1(c), respectively).

In the H^+-$OH_{\parallel}$ configuration the resulting OH bond was rather short; equal to 0.95 Å. The Be nearest neighbor of H^+ eventually displaced far away from H^+ along the **c** axis (the final H-Be distance was equal to 1.73 Å) and approached another oxygen nearby (denoted by the asterisk in Fig. 1(b)) forming a new Be-O bond. The result of such a rebonding was that this Be ion preserved its four-fold coordination as in the bulk crystal. In contrast, the oxygen ion forming the initial dative OH bond has lost one of its four Be neighbors. Effectively, the H^+ incorporation, therefore, leads to the breaking of the initial Be-O bond and formation of a new one. On the other hand, in the H^+-$OH_{\perp}$ configuration the original Be-O bond still persists, owing to the concerted displacements of both H^+ and Be which although repel each other manage to relocate at positions that allow the preservation of the initial Be-O bond (with a length equal to 1.77 Å; see Fig. 1(c)). In the final relaxed state the OH bond length is equal to 0.985 Å.

In contrast, the antibonding AB-O sites were found to be locally stable sites with rather minimal structural relaxation. The two distinct configurations in this case comprise the one with the OH bond parallel (H^+-$ABO_{\parallel}$) and the other with the OH bond nearly perpendicular to the **c** axis (H^+-$ABO_{\perp}$) (see Fig. 1(d) and Fig. 1(e), respectively). In either case the corresponding OH lengths were equal to 0.98 Å. Also, in both cases the initial Be-O bonds

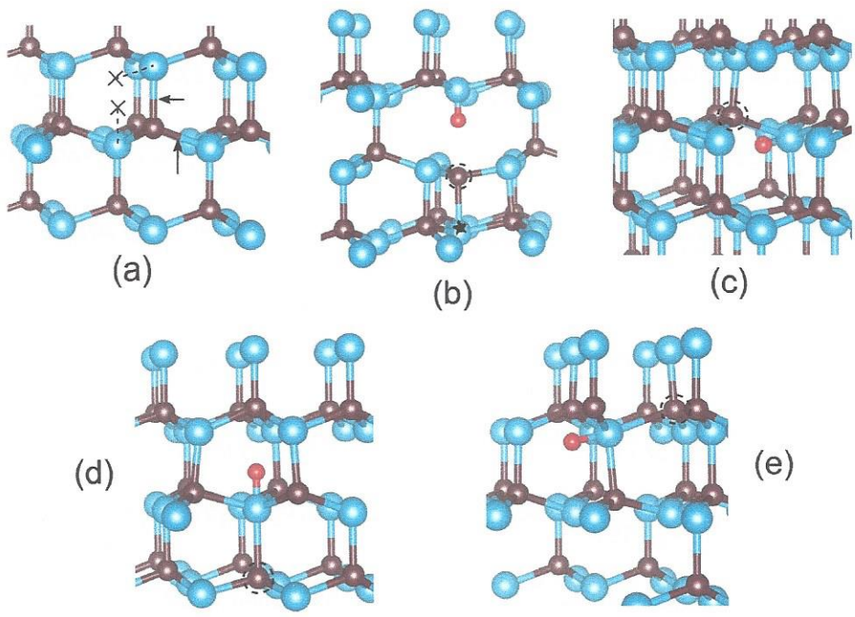

FIG. 1. Stable hydrogen configurations in its positively-charged state H^+ determined from the hybrid-functional calculations. (a) Part of the bulk crystalline BeO supercell showing the BC and AB-O sites. The positions of the BC sites are shown by the arrows, whereas those of the AB-O sites by the $\times$ symbols. (b) Bond-type configuration, H^+-$OH_{\|}$, with OH bond parallel to the **c** axis. The asterisk denotes the oxygen atom which forms the newly formed Be-O bond after the introduction of the hydrogen at the BC site of the original Be-O bond. (c) Bond-type configuration, H^+-$OH_{\perp}$, with OH bond almost perpendicular to the **c** axis. (d) Bond-type configuration H^+-$ABO_{\|}$ with H^+ at the AB-O site with the OH bond parallel to the **c** axis. (e) Bond-type configuration H^+-$ABO_{\perp}$ with H^+ at the AB-O site with the OH bond almost perpendicular to the **c** axis. Elements are represented as: H (small red sphere), Be (small dark-brown spheres), O (large blue spheres). The circled (by dashed lines) Be ions denote the Be ions of the original Be-O bonds.

persisted until the end of the relaxation. The only exception was the Be-O length in the H^+-$ABO_{\perp}$ configuration which sustained some elongation, with a final length of 1.88 Å in the relaxed structure (see Fig. 1(e)). Finally, the AB-Be site for H^+ proved to be unstable with the hydrogen displacing away and finally occupying the H^+-$OH_{\|}$ site.

The bond-type H^+-$OH_{\|}$ configuration with the OH bond parallel to the **c** axis is predicted to be the ground state (with the lowest formation energy) of H^+ for either functional (see

TABLE I. Formation energies of the different positively-charged hydrogen configurations in BeO, obtained by both PBE and HSE06 functionals. Energies (in eV) are referenced with respect to the formation energy of the ground-state configuration.

	PBE	HSE06
H^+-$OH_{\parallel}$	0.00	0.00
H^+-$ABO_{\perp}$	0.44	0.46
H^+-$OH_{\perp}$	0.45	0.54
H^+-$ABO_{\parallel}$	0.62	0.65

Table I). Furthermore, as it can be seen from the same Table, the PBE functional reproduces the HSE06 energy differences between H^+-$OH_{\parallel}$ and the higher-energy structures with a good accuracy.

Hydrogen in its neutral state, H^0, displayed important differences with respect to H^+ by stabilizing at different positions in the lattice. Among the different neutral configurations resolved, the lowest-energy one (ground state) was an interstitial configuration with hydrogen residing at the existing empty interstitial sites of the host lattice, avoiding close proximity with other ions of the host (see Fig. 2(a) and Fig. 2(b)). More specifically, the three nearest Be ions to the hydrogen are found at 1.67 Å away, whereas the nearest oxygen ions are located a bit further away: at 1.88 Å (three oxygen ions) and at 1.99 Å (three more distant oxygen ions). These interstitial sites are of high-symmetry and define the centers of the hexagonal rings when viewed along the crystallographic **c** axis (see Fig. 2(b)). A similar situation occurs for the highly-ionic alkaline-earth oxide MgO where neutral hydrogen also was found to reside at empty interstitial sites.[61–63]

In contrast to MgO, however, H^0 was further found to adopt additional stable configurations, in particular after neutralizing the positively-charged H^+-$OH_{\parallel}$ and H^+-$OH_{\perp}$ structures by addition of an electron and then initiating the energy minimization. Both of them stabilized eventually to neutral elongated-bond type configurations with an equilibrium OH bond length equal to 1.26 Å (see Fig. 2(c) and Fig. 2(d)). The nearest Be ion of the initial Be-O bond was found at a distance of 1.37 Å away from hydrogen in either case. The existence of such elongated-bond configurations (as opposed to MgO[61–63]) is very likely a signature of the

presence of the covalent character of bonding for BeO, something that has been argued in early Hartree-Fock calculations.[2] In that study the calculated charge-density maps revealed a finite concentration of electrons along the lines connecting the Be and O species.[2] The stability of these elongated-bond configurations was also verified by calculations employing the HSE06 functional where indeed they were found to be local-energy minima with vanishing forces (see Table II). A fourth distinct H^0 configuration was also resolved with a distance of 1.51 Å between hydrogen and the nearest oxygen ion (see Fig. 2(e)). This structure was the outcome of the relaxation after placing hydrogen at the AB-O site with the initial Be-O bond oriented parallel to the **c** axis.

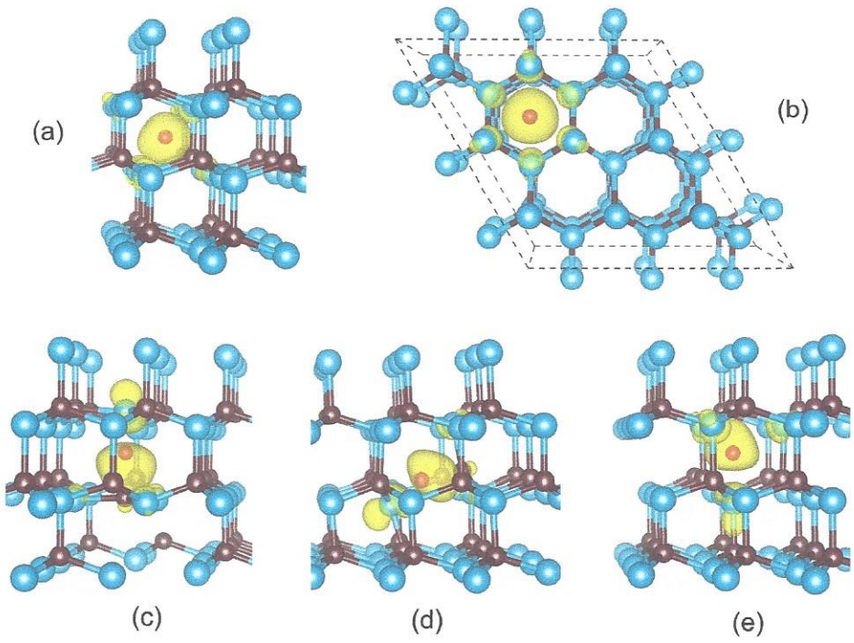

FIG. 2. Stable neutral hydrogen configurations and their spin-density isosurface (depicted in yellow) as obtained from the hybrid-functional calculations. The isosurface value was 0.007 au^{-3}. (a) Ground-state interstitial configuration H^0_{int}; view perpendicular to the **c** axis. (b) Ground-state interstitial configuration H^0_{int}; view parallel to the **c** axis. (c) Elongated-bond-type configuration, H^0-$OH_{\parallel}$, with OH bond parallel to the **c** axis. (d) Elongated-bond-type configuration, H^0-$OH_{\perp}$, with OH bond almost perpendicular to the **c** axis. (e) Higher-energy interstitial configuration H^0_{int2}; view perpendicular to the **c** axis. Elements are represented as: H (small red sphere), Be (small dark-brown spheres), O (large blue spheres).

Hydrogen stabilizes in a single unique configuration in its negatively-charged state, H^-. The hydrogen nucleus occupies the high-symmetry interstitial site in the lattice at the centers of the hexagonal rings, similarly to the neutral H^0_{int} configuration, albeit with some differences in the local topology. More specifically, examination of the local environment showed that the presence of hydrogen at this site maximizes H-O distances with the nearest oxygen ions (they become larger than 2.00 Å), whereas the nearest Be ions (three in total) are found at 1.455 Å away.

Taking the lowest-energy configuration for each charge state q of hydrogen the corresponding formation energies were calculated as a function of the Fermi-level position in the gap. The formation-energy plot in Fig. 3 shows the corresponding results obtained with the HSE06 functional. The vertical lines denote the positions of the thermodynamic charge-transition levels, $E(q, q')$. It can be inferred that hydrogen possesses deep donor E(+/0) and acceptor E(0/-) levels, both found considerably away from the respective band edges. More, specifically: E(+/0) = E_C - 3.90 eV) and E(0/-) = E_V + 5.51 eV. The pinning level, E(+/-), similarly lies at the mid-gap region (E(+/-) = E_V + 6.09 eV), showing that hydrogen is an amphoteric defect in BeO, namely it cannot act as a source of carriers at conditions of thermodynamic equilibrium. Instead, it will counteract the prevailing type of conductivity in the solid by releasing electrons (holes) at p-type (n-type) conditions. The specific ordering of the transition levels (the donor level lying higher in the gap with respect to the acceptor level) also imply that hydrogen is a negative-U defect and the neutral charge state, H^0, is never the lowest-energy state at thermodynamic equilibrium. However, techniques such as μSR spectroscopy can access the paramagnetic neutral state since they can probe short-lived transient states which do not require long equilibration times.

B. Electronic structure and hyperfine parameters of neutral hydrogen

Inspection of the energies of the single-particle electron states for all H^0 configurations showed that the presence of hydrogen induces deep energy levels inside the band gap. The location of these levels (as obtained by the HSE06 functional) are depicted schematically in Fig. 4 for each distinct configuration. The level positions for both spin channels are shown. It can be seen that all occupied levels are located in the lower half of the gap; the lower-lying one closer to the valence band is the defect level for the ground-state H^0_{int} configuration.

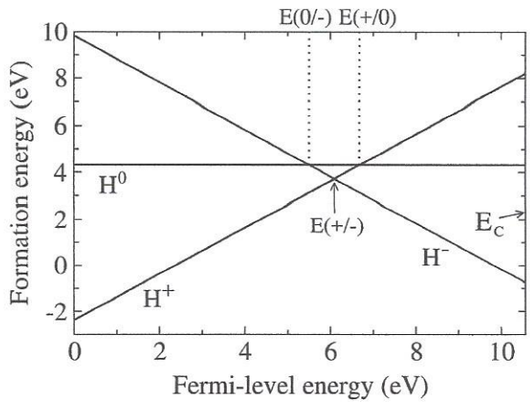

FIG. 3. Formation-energy plot of the charged states of hydrogen as a function of the Fermi-level position in the gap. For each charge state the corresponding energy of the lowest-energy (ground-state) configuration is used. The results were obtained from the hybrid-functional (HSE06) approach. The vertical lines denote the thermodynamic charge-transition levels. The reference energy for the Fermi level is set at the valence-band edge (E_V) of the bulk supercell. E_C marks the position of the conduction-band minimum.

The spin-density isosurfaces for all neutral configurations of hydrogen are also depicted in Fig. 2. It is clear that all of these configurations possess rather compact densities localized at the hydrogen site and its immediate vicinity. The ground-state H^0_{int} is seen to possess a localized and spherically-symmetric electron distribution of s character centered on the hydrogen site, in fact resembling a trapped-atom configuration. The calculation of the hyperfine tensor for H^0_{int} revealed a very high value for the Fermi-contact isotropic component (A_{iso}) and negligible anisotropic contribution, suggesting a prominent atomlike character (see Table II). More specifically, the calculated magnitude of A_{iso} for H^0_{int} equals 1329 and 1460 MHz by PBE and HSE06, respectively. These high values reflect the strong atomlike character of H^0_{int} approaching (and even surpassing for the case of HSE06) the vacuum value of A_{iso} (1420 MHz) for a free hydrogen atom.[58]

Table II also lists the calculated hyperfine parameters (both isotropic and dipolar constants) for all stable H^0 configurations. Similarly to earlier studies[57,64] it was found necessary to increase the plane-wave cutoff considerably in order to obtain converged isotropic constants, A_{iso}. For the case of the semi-local PBE functional a value of 650 eV led to converged A_{iso}'s to within $\pm$ 10 MHz. The respective PBE values at the lower cutoff (550 eV) are also

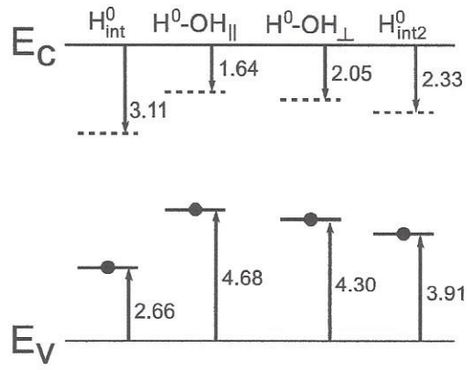

FIG. 4. Positions of defect-induced levels in the gap for the various neutral H^0 hydrogen configurations obtained from spin-polarized hybrid-functional (HSE06) calculations. Solid (dashed) lines denote the occupied (unoccupied) levels of the spin-up (spin-down) channels. The corresponding energy distances (in eV) with respect to the valence-band (conduction-band) edges are displayed for each occupied (unoccupied) level.

listed (in parentheses). In contrast, the dependency of the magnitude of the dipolar hyperfine constants D upon the plane-wave cutoff is much weaker. The more elaborate HSE06 hyperfine calculations were completed using the smaller cut-off (550 eV). Therefore, any quantitative comparison among PBE and HSE06 for the hyperfine constants could only be made at 550 eV.

In contrast to the atomlike H^0_{int} configuration, the two elongated-bond configurations possess considerably smaller isotropic hyperfine parameters (693 and 655 MHz from HSE06; slightly less than 50% of the vacuum value) and were also characterized by a sizeable axially-symmetric dipolar part, in the range of 50 to 60 MHz irrespective of the specific functional employed (see Table II). These values confirm the spin-density distributions for both of these configurations where a strong degree of delocalization can be seen towards the neighboring oxygen ion O_{NN} of the elongated OH bond (see Fig. 2(c) and Fig. 2(d)). The finite spin density at the O_{NN} ion should probably be understood as the effect of the presence of the impurity polarizing its immediate environment. Population analysis revealed that the electron density centered at O_{NN} is of p character. The existence of the elongated O-H bond imposes a degree of anisotropy to the hyperfine coupling leading to a finite axially-symmetric anisotropic part with the O_{NN}-H bond defining the axis of symmetry of the

hyperfine interaction.

Finally, the higher-energy interstitial configuration H^0_{int2} was found to possess a very high isotropic constant, A_{iso}, by either functional, albeit smaller than the one of the interstitial H^0_{int} state (see Table II). This is not surprising, since H^0_{int2} has also a strong atomlike character with the majority of the spin density centered on the hydrogen nucleus (see Fig. 2(e)). Some degree of polarization is also evident with residual spin density present on the nearest oxygen ion, again of *p*-type character. A finite dipolar parameter of axial symmetry of about 5 MHz was also obtained for H^0_{int2} by either functional (see Table II).

Comparison of the PBE and HSE06 results for the hyperfine constants at the lower plane-wave cutoff of 550 eV (see Table II) shows that the PBE functional underestimates systematically the magnitude of the isotropic constant, A_{iso}, for all distinct H^0 configurations. Very likely this is related to the known tendency of semi-local and local density functionals to favor more delocalized electron densities in solids.[31] This delocalization effectively leads to smaller spin densities at the sites of the nuclei, thus leading to smaller hyperfine constants A_{iso}. For the case of the dipolar constants, instead, the PBE results reproduce well the HSE06 ones (see Table II).

TABLE II. Formation energies (in eV) and hyperfine constants (in MHz) of the different neutral hydrogen configurations in BeO, obtained by the PBE and HSE06 functionals. The formation energy of the ground-state configuration (H^0_{int}) provides the reference energy for the quoted energies. The hyperfine constants were obtained using plane-wave cut-offs of 650 eV and 550 eV for the PBE and HSE06 functionals, respectively. The corresponding hyperfine constants at 550 eV obtained by the PBE functional are also shown inside parentheses.

	PBE			HSE06		
	ΔE_{form}	A_{iso}	D	ΔE_{form}	A_{iso}	D
H^0_{int}	0.00	1329 (1315)	- (-)	0.00	1460	-
H^0-$OH_{\parallel}$	0.73	670 (660)	51 (51)	0.99	693	60
H^0-$OH_{\perp}$	0.89	605 (599)	54 (54)	1.13	655	56
H^0_{int2}	1.15	1171 (1169)	4.5 (4.5)	1.41	1307	5

C. μSR results

The oxide sample used in the present study was a high-purity single crystal grown by V.A. Maslov using a modified solution-melt method under reverse temperature drop conditions.[65] Muon spin rotation experiments were performed in the HAL9500 instrument of the Laboratory for Muon Spectroscopy at the Paul-Scherrer Institut (Villigen, Switzerland). Positive muons with nearly 100% spin-polarization were implanted in the sample at $T = 6$ K. A high external magnetic field was applied perpendicular to the initial muon spin polarization.

Fast-Fourier transforms (FFT) of the μSR spectra obtained at fields ranging from $B = 1$ T to $B = 8$ T are shown in Fig. 5. The FFT spectra clearly show the presence of three lines corresponding to oscillations of the detected muon spin polarization. The lowest frequency corresponds to the expected Larmor frequency of the muon subject to a diamagnetic environment, $\nu_{dia} = \gamma_\mu B$, where $\gamma_\mu = 135.53$ MHz/T is the gyromagnetic ratio of the muon. The two frequencies observed at higher frequencies correspond to muons in a paramagnetic environment and, as we will detail below, correspond to the ν_{12} and ν_{34} transitions of a muonium state with a vacuum-like hyperfine interaction. The smaller amplitude of the ν_{34} line with respect to that of the ν_{12} line (Fig. 5) reflects the time resolution of the detector system.

The time spectra were therefore analysed using a sum of damped oscillations of the form:

$$\begin{aligned} A(t) = A_{\mathrm{dia}} e^{-\lambda_{\mathrm{dia}} t} \cos\left(2\pi\nu_{\mathrm{dia}} t + \phi_{\mathrm{dia}}\right) \\ + A_{12} e^{-\lambda_{12} t} \cos\left(2\pi\nu_{12} t + \phi_{12}\right) \\ + A_{34} e^{-\lambda_{34} t} \cos\left(2\pi\nu_{34} t + \phi_{34}\right) \end{aligned}$$

The asymmetry parameters A_{dia}, A_{12} and A_{34} are highly frequency-dependent at these applied high fields, but the similarity of the ν_{dia} and ν_{12} frequencies at $B = 8$ T allow the comparison of the fitted A_{dia} and A_{12} with the corresponding value A_{max} for a silver calibration run at the same field. We thus estimate a diamagnetic fraction $f_{dia} = A_{dia}/A_{max} = 14.1(1)\%$ and a muonium fraction $f_{Mu} = 2 \times A_{12}/A_{max} = 42.2\%$, where we multiply A_{12} by 2 in order to take into account the corresponding muonium fraction associated to the ν_{34} line. We note that 43.7(2)% of the muon spin polarization is not observed at this temperature and field, corresponding either to a third configuration and/or to the presence of dynamical processes

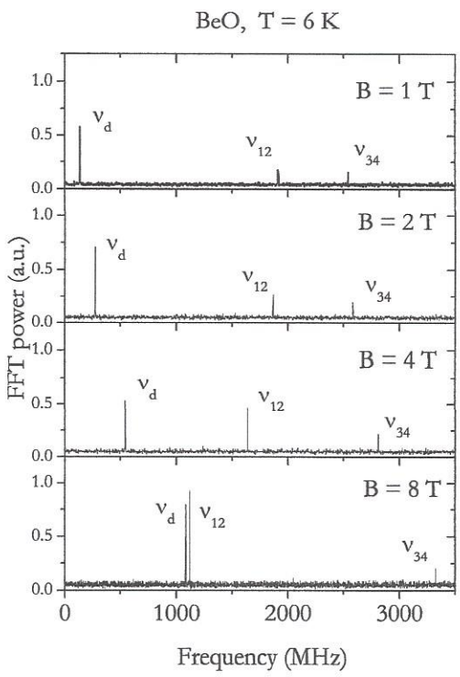

FIG. 5. Fast-Fourier transforms (FFT) of the μSR spectra obtained at fields ranging from $B = 1$ T to $B = 8$ T, at $T = 6$ K. Three lines are clearly visible: ν_d corresponds to a diamagnetic state; ν_{12} and ν_{34} correspond to a muonium state with a vacuum-like hyperfine interaction, as discussed in the text.

associated to the muon thermalization.[66–68] The fitted frequencies ν_{12} and ν_{34} are plotted in Fig. 6 and consistently behave as the hyperfine transitions of an isotropic muonium state with a vacuum-like hyperfine parameter. According to this model we expect:[69]

$$\nu_{12} = \left| \frac{A_{iso}}{2} + \nu_- - \frac{\nu_+}{\beta} \right|$$
$$\nu_{34} = \left| \frac{A_{iso}}{2} - \nu_- + \frac{\nu_+}{\beta} \right|$$

where $A_{\rm iso}$ is the hyperfine parameter, $\nu_\pm = (\gamma_e \pm \gamma_\mu)B/2$, (with $\gamma_e = 28024.21$ MHz/T and $\gamma_\mu = 135.53$ MHz/T), and $\beta = \sqrt{1 + (A_{iso}/2\nu_+)^2}$. The lines in Fig. 6 are a global fit to this model with the hyperfine

parameter $A_{\rm iso}$ as the single fitting parameter. The fit yields $A_{\rm iso}$(Mu) = 4451.2(2) MHz. We recall that the hyperfine interaction for muonium is expected to be higher than that for hydrogen by the factor 3.184 corresponding to the ratio of the magnetic moment of the muon and that of the proton.[20] The expected value for the hyperfine interaction of the hydrogen state corresponding to our observed muonium state is therefore $A_{\rm iso}$(H) = 1398.00(6) MHz. This value compares very well with the calculated values, both by PBE and HSE06 for the $H^0_{\rm int}$ ground-state configuration. The experimentally determined value of the hyperfine interaction is about 6% larger than that calculated with PBE and 6% smaller than that calculated with HSE06 for the same configuration. These small discrepancies are in line with the smallest found between calculated and measured hyperfine interactions in solids.[25,53,57,58] A slight variation of the value of the hyperfine interaction of muonium with respect to that of hydrogen is also expected due to the different zero-point motion of the muon and of the proton.

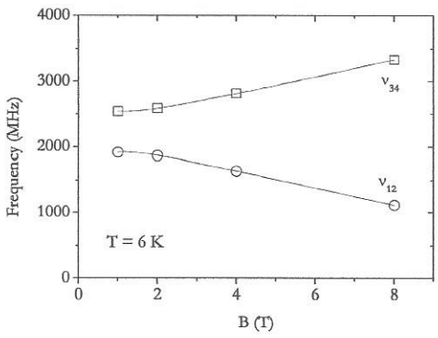

FIG. 6. Frequencies ν_{12} and ν_{34} as a function of applied transverse magnetic field, as obtained from the fits to the time spectra. The lines are a global fit to an isotropic muonium state with the hyperfine parameter $A_{\rm iso}$ as the single fitting parameter, resulting in $A_{\rm iso}$ = 4451.2(2) MHz.

We note that a small fraction of the muons thermalize on a diamagnetic fraction, which likely corresponds to Mu^+ stopping in one of the configurations shown in Fig. 1. Our experimental results do not allow a site assignment. However, we recall that the bond-type ground-state configuration implies a strong local rearrangement around the proton/muon, whereas the antibonding configurations imply a minimal local impact of the impurity (see Fig.1). It is therefore likely that at low temperatures and in the lifetime of the muon there is no

place for the strong atomic changes required to achieve the ground state, and that the muon thermalizes instead at some of the less-stressed antibonding configurations. Similarly, in I-III-VI_2 chalcopyrite semiconductors derived from the II-VI structures, Mu^+ has been determined by μSR to be at an anion antibonding site,[70,71] whereas the calculated ground state H^+ site was found at the bond center by ab-initio calculations.[72] This divergence on the site between theory and experiment has remained unexplained. However, as we now find in BeO, it is likely that also in these ternary semiconductors the local rearrangement needed to achieve the ground-state configuration can not be attained during the time of the muon implantation, thermalization and decay.

IV. CONCLUSIONS

First-principles calculations based on the semi-local PBE and hybrid HSE06 functionals showed that hydrogen is an amphoteric defect in BeO with deep acceptor and donor levels similarly to its behavior in MgO, the other wide-gap alkaline-earth oxide. In contrast to the strongly ionic MgO, however, hydrogen was further found to be stable in a few other minimum-energy configurations for the case of the neutral paramagnetic H^0 state, a finding that should be justified from the presence of a small covalent character of bonding which stabilizes elongated OH-bond configurations.

All distinct H^0 configurations introduced deep defect levels lying in the lower half of the gap and were characterized by localized spin densities at and near the impurity. The ground-state interstitial configuration H^0_{int}, in particular, resembles strongly a trapped-atom configuration with the spin density centered on the hydrogen nucleus. The calculations by either functional revealed a very high isotropic hyperfine interaction for this configuration with a magnitude of A_{iso} near the vacuum value. In contrast, the other configurations displayed spin delocalization to the oxygen nearest neighbor which for the elongated-bond configurations gave rise to a sizable dipolar part of axial symmetry and much smaller A_{iso} values. The μSR data verify the ab initio calculations by resolving a neutral muonium fraction with a vacuum-like hyperfine constant. The value for the hyperfine constant of the corresponding hydrogen state is 1398 MHz (after correcting for the ratio of the magnetic moments of the proton and of the muon), and agrees favorably with the A_{iso} values predicted for the lowest-energy interstitial H^0_{int} state by both PBE and HSE06 functionals.

V. ACKNOWLEDGMENTS

This work was supported with funds from (i) FEDER (Programa Operacional Factores de Competitividade COMPETE) and from FCT Portugal - Fundação para a Ciência e Tecnologia under projects UID/FIS/04564/2016 and PTDC/FIS/102722/2008; (ii) PhD grant SFRH/BD/87343/2012 from FCT - Fundação para a Ciência e Tecnologia (RBLV); (iii) RFBR (14-02-00080, 14-03-00121 and 16-29-06410) (MVY); (iv) UB RAS (grant 15-20-3-11) (MVY); (v) Act 211 of the Government of Russia 02.A03.21.0006 (MVY). The computer resources of the Department of Physics of the University of Coimbra were used, including the Milipeia cluster at the Laboratory for Advanced Computing. The technical help of the μSR team at PSI is gratefully acknowledged.

REFERENCES

[1] *High Temperature Oxides, Part III. Magnesia, Alumina, Beryllia Ceramics, Fabrication, Characterization and Properties.* A. M. Alper Ed. Vol. 5-III of *Refractory Materials* (Academic Press, New York and London, 1970).

[2] A. Lichanot, M. Chaillet, C. Larrieu, R. Dovesi, and C. Pisani, Chemical Physics **164**, 383 (1992).

[3] K. B. Joshi, R. Jain, R. K. Pandya, B. L. Ahuja, and B. K. Sharma, J. Chem. Phys. **111**, 163 (1999).

[4] D. A. Ditmars and D. C. Ginnings, J. Res. Nat. Bureau Standards **59**, 93 (1957).

[5] A. M. C. Santos, M. Mohammadi, V.S. Afshar, Radiation Measurements, **17**, 1 (2015).

[6] A. Allouche and Y. Ferro, Solid State Ionics **272** 91 (2015).

[7] M. Lei, J. H. Yum, T. W. Hudnall, C. W. Bielawski, S. K. Banerjee, P. S. Lysaght, G. Bersuker, and M. C. Downer, Appl. Phys. Lett. **100**, 122906 (2012).

[8] J. H. Yum, T. Akyol, D. A. Ferrer, J. C. Lee, S. K. Banerjee, M. Lei, M. Downer, T. W. Hudnall, C. W. Bielawski, and G. Bersuker, J. Vac. Sci. Technol. A **29** 061501 (2011).

[9] D. M. Fleetwood, Microelectronics Reliability **42**, 523 (2002).

[10] D. K. Schroder and J. A. Babcock, J. Appl. Phys. **94**, 1 (2003).

[11] M. Houssa, G. Pourtois, M. M. Heyns, and A. Stesmans, J. Phys.: Condens. Matter **17**, S2075 (2005).

[12]S. T. Pantelides, L. Tsetseris, S. N. Rashkeev, X. J. Zhou, D. M. Fleetwood, and R. D. Schrimpf, Microelectronics Reliability **47**, 903 (2007).

[13]M. S. Khalil, M. J. A. Stoutimore, S. Gladchenko, A. M. Holder, C. B. Musgrave, A. C. Kozen, G. Rubloff, Y. Q. Liu, R. G. Gordon, J. H. Yum, *et al.*, Appl. Phys. Lett. **103**, 162601 (2013).

[14]D. Koh, J.-H. Yum, S. K. Banerjee, T. W. Hudnall, C. Bielawski, W. A. Lanford, B. J. French, M. French, P. Henry, H. Li, M. Kuhn, and S. W. King, J. Vac. Sci. Technol. B **32**, 03D117 (2014).

[15]P. Hohenberg and W. Kohn, Phys. Rev. **136**, B864 (1964).

[16]W. Kohn and L. J. Sham, Phys. Rev. **140**, A1133 (1965).

[17]J. P. Perdew, K. Burke, and M. Ernzerhof, Phys. Rev. Lett. **77**, 3865 (1996).

[18]J. S. Lord, S. P. Cottrell, P. J. C. King, H. V. Alberto, N. Ayres de Campos, J. M. Gil, J. Piroto Duarte, R. C. Vilão, R. L. Lichti, S. K. L. Sjue, B. A. Bailey, A. Weidinger, E. A. Davis, and S. F. J. Cox, Physica B: Condensed Matter **308-310**, 920 (2001).

[19]J. M. Gil, H. V. Alberto, R. C. Vilão, J. Piroto Duarte, N. Ayres de Campos, A. Weidinger, E. A. Davis, and S. F. J. Cox, J. Phys.: Condens. Matter **13**, L613 (2001).

[20]R. C. Vilão, R. B. L. Vieira, H. V. Alberto, J. M. Gil, A. Weidinger, R. L. Lichti, B. B. Baker, P. W. Mengyan, and J. S. Lord, Phys. Rev. B **92**, 081202 (2015).

[21]R. L. Lichti, K. H. Chow, J. M. Gil, D. L. Stripe, R. C. Vilão, and S. F. J. Cox, Physica B: Condensed Matter **376-377**, 587 (2006).

[22]S. F. J. Cox, J. L. Gavartin, J. S. Lord, S. P. Cottrell, J. M. Gil, H. V. Alberto, J. Piroto Duarte, R. C. Vilão, N. Ayres de Campos, D. J. Keeble, E. A. Davis, M. Charlton, and D. P. van der Werf, J. Phys.: Condens. Matter **18**, 1079 (2006).

[23]R. C. Vilão, A. G. Marinopoulos, R. B. L. Vieira, A. Weidinger, H. V. Alberto, J. Piroto Duarte, J. M. Gil, J. S. Lord, and S. F. J. Cox, Phys. Rev. B **84**, 045201 (2011).

[24]E. L. Silva, A. G. Marinopoulos, R. C. Vilão, R. B. L. Vieira, H. V. Alberto, J. Piroto Duarte, and J. M. Gil, Phys. Rev. B **85**, 165211 (2012).

[25]E. L. Silva, A. G. Marinopoulos, R. B. L. Vieira, R. C. Vilão, H. V. Alberto, J. M. Gil, R. L. Lichti, P. W. Mengyan, and B. B. Baker, Phys. Rev. B **94**, 014104 (2016).

[26]R. B. L. Vieira, R. C. Vilão, A. G. Marinopoulos, P. M. Gordo, J. A. Paixão, H. V. Alberto, J. M. Gil, A. Weidinger, R. L. Lichti, B. Baker, P. W. Mengyan, and J. S. Lord, Phys. Rev. B **94**, 115207 (2016).

[27]G. Pacchioni, F. Frigoli, D. Ricci, and J. A. Weil, Phys. Rev. B **63**, 054102 (2000).

[28]J. Laegsgaard and K. Stokbro, Phys. Rev. Lett. **86**, 2834 (2001).

[29]M. d'Avezac, M. Calandra, and F. Mauri, Phys. Rev. B **71**, 205210 (2005).

[30]M. Cococcioni and S. de Gironcoli, Phys. Rev. B **71**, 035105 (2005).

[31]S. Lany and A. Zunger, Phys. Rev. B **80**, 085202 (2009).

[32]S. Duman, A. Sütlü, S. Bağci, H. M. Tütüncü, and G. P. Srivastava, J. Appl. Phys. **105**, 033719 (2009).

[33]Z.-C. Guo, F. Luo, G.-F. Ji, L.-C. Cai, and Y. Cheng, Physica B **438**, 60 (2014).

[34]M. Shahrokhi and C. Leonard, J. Alloys and Compounds **682**, 254 (2016).

[35]K. J. Chang, S. Froyen, and M. L. Cohen, J. Phys. C: Solid State Phys. **16**, 3475 (1983).

[36]Y.-N. Xu and W. Y. Ching, Phys. Rev. **48**, 4335 (1993).

[37]B. Baumeier, P. Krüger, and J. Pollmann, Phys. Rev. **75**, 045323 (2007).

[38]D. M. Roessler and W. C. Walker, J. Phys. Chem. Solids **30**, 157 (1969).

[39]D. Groh, R. Pandey, M. B. Sahariah, E. Amzallag, I. Baraille, and M. Rérat, J. Phys. Chem. Solids **70**, 789 (2009).

[40]J. Heyd and G. E. Scuseria, The Journal Chem. Phys. **121**, 1187 (2004).

[41]J. Paier, M. Marsman, K. Hummer, G. Kresse, I. C. Gerber, and J. G. Angyan, The Journal Chem. Phys. **124**, 154709 (2006); **125**, 249901 (2006).

[42]M. Marsman, J. Paier, A. Stroppa, and G. Kresse, J. Phys.: Condens. Matter **20**, 064201 (2008).

[43]S. F. J. Cox, R. L. Lichti, J. S. Lord, E. A. Davis, R. C. Vilão, J. M. Gil, T. D. Veal, and Y. G. Celebi, Physica Scripta **88**, 068503 (2013).

[44]R. C. Vilão, J. M. Gil, A. Weidinger, H. V. Alberto, J. Piroto Duarte, N. Ayres de Campos, R. L. Lichti, K. H. Chow, and S. F. J. Cox, Nuclear Instruments and Methods in Physics Research Section A **580**, 438 (2007).

[45]A. Stoykov, R. Scheuermann, K. Sedlak, J. Rodriguez, U. Greuter, and A. Amato, Physics Procedia **30**, 7 (2012).

[46]A. Suter and B. M. Wojek, Physics Procedia **30**, 69 (2012).

[47]P. E. Blöchl, Phys. Rev. B **50**, 17953 (1994).

[48]G. Kresse and D. Joubert, Phys. Rev. B **59**, 1758 (1999).

[49]G. Kresse and J. Hafner, Phys. Rev. B **47**, 558 (1993).

[50]G. Kresse and J. Hafner, Phys. Rev. B **49**, 14251 (1994)

[51]G. Kresse and J. Furthmüller, Phys. Rev. B **54**, 11169 (1996).

[52]P. E. Blöchl, Phys. Rev. B **62**, 6158 (2000).

[53]K. Szász, T. Hornos, M. Marsman, and A. Gali, Phys. Rev. B **88**, 075202 (2013).

[54]G. Makov and M. C. Payne, Phys. Rev. B **51**, 4014 (1995).

[55]E. Loh, Phys. Rev. **166**, 673 (1968).

[56]A. Bosak, K. Schmalzl, M. Krisch, W. van Beek, and V. Kolobanov, Phys. Rev. B **77**, 224303 (2008).

[57]C. G. Van de Walle, Phys. Rev. Lett. **64**, 669 (1990).

[58]C. G. Van de Walle and P. E. Blöchl, Phys. Rev. B **47**, 4244 (1993).

[59]J. M. Spaeth and H. Overhof, *Point Defects in Semiconductors and Insulators*, Vol. 51 of *Springer Series in Materials Science*, (Springer, 2003).

[60]G. A. Jeffrey, G. S. Parry, and R. L. Mozzi, J. Chem. Phys. **25**, 1024 (1956).

[61]H. Li and J. Robertson, J. Appl. Phys. **115**, 203708 (2014).

[62]Ç. Kiliç and A. Zunger, Appl. Phys. Lett. **81**, 73 (2002).

[63]K. Xiong, J. Robertson, and S. J. Clark, J. Appl. Phys. **102**, 083710 (2007).

[64]A. G. Marinopoulos, J. Phys.: Condens. Matter **26**, 025502 (2014).

[65]V. A. Maslov, G. M. Bylov, B. G. Mazurenko, A. V. Kruzhalov, and B. V. Shulgin, Proc. 6$^{\text{th}}$ Int. Conference on Crystal Growth, Vol. 3 (Moscow, 1980) p. 268-269.

[66]H. V. Alberto, A. Weidinger, R. C. Vilão, J. Piroto Duarte, J. M. Gil, J. S. Lord, and S. F. J. Cox, Phys. Rev. B **81**, 245205 (2010).

[67]H. V. Alberto, R. C. Vilão, J. Piroto Duarte, J. M. Gil, A. Weidinger, J. S. Lord, and S. F. J. Cox, Phys. Rev. B **86**, 035203 (2012).

[68]R. B. L. Vieira, R. C. Vilão, H. V. Alberto, J. M. Gil, A. Weidinger, B. B. Baker, P. W. Mengyan, and R. L. Lichti, J. of Physics: Conference Series **551**, 012048 (2014).

[69]B. D. Patterson, Rev. Mod. Phys. **60**, 69 (1988).

[70]J. M. Gil, P. J. Mendes, L. P. Ferreira, H. V. Alberto, R. C. Vilão, N. Ayres de Campos, A. Weidinger, Y. Tomm, Ch. Niedermayer, M. V. Yakushev, R. D. Tomlinson, S. P. Cottrell, and S. F. J. Cox, Phys. Rev. B **59**, 1912 (1999).

[71]R. C. Vilão, J. M. Gil, H. V. Alberto, J. Piroto Duarte, N. Ayres de Campos, A. Weidinger, M. V. Yakushev, and S. F. J. Cox, Physica B: Condensed Matter **326**, 181 (2003).

[72]Ç. Kiliç and A. Zunger, Phys. Rev. B **68**, 075201 (2003).